Spatially-Adaptive Advection Radar Technique for Precipitation Mosaic Nowcasting

Mario Montopoli, Frank Silvio Marzano, *Senior Member, IEEE*, Errico Picciotti, and Gianfranco Vulpiani, *Member, IEEE*

***Abstract*—A new numerical nowcasting technique to predict the radar reflectivity field at very short term, up to few hours, is presented. The method is based on the spatial segmentation of the reflectivity field and estimated advection field to produce radar reflectivity forecasts and, for this reason, is named Spatially-adaptive Precipitation Advective Radar Estimator (SPARE). A large data set coming from the Italian radar network mosaic (spatial domain size of about 1200×1200 km^2) is used to test the overall performance of SPARE against the simplest method of radar map temporal persistence. An original approach to estimate the radar field motion, based on the phase cross-correlation principle, is formulated in this paper. Results are given either in terms of skill scores of predicted radar maps or in terms of predicted uncertainty. The latter provides a new methodology to evaluate the expected performance of SPARE predictions.**

***Index Terms*—Advection scheme, ground based weather radar, short term prediction.**

I. Introduction

FORECAST of rainfall is usually performed by Numerical Weather Prediction (NWP) models which allow obtaining a reliable description of the state of the atmosphere up to several hours ahead [14]. Due to their physical basis, these models are able to describe the formation of precipitation systems at mesoscale, but often fail to forecast them at smaller scales and short time due to either their coarse temporal and spatial resolution, or to their approximate dynamics and microphysics (e.g., [2], [7]). Many practical applications, e.g., in the fields of hydrology, civil protection and flight assistance, require quantitative precipitation forecasts (QPF) at high resolution in space and time. To this aim, many efforts have been recently carried out to improve forecast skills at very short time (i.e., up to a few hours). using nowcasting algorithms. Nowcasting, i.e., very short-term prediction, is usually based on observations exclusively. It can be thought as a faster and easier alternative to rigorous assimilation techniques which allow the forecast improvement by including observations into NWP models at the expense of the computational time [5], [12].

Nowcasting methods, based on radar data time series, can be divided into three categories: i) extrapolation and recognition techniques; ii) dynamical evolution techniques; iii) hybrid methods which combine radar information with external data sources.

The first class of nowcasting algorithms is aimed at tracing the precipitation temporal path guaranteeing the best spatial coherence of the predicted field. These algorithms extrapolate observed precipitation fields to successive time periods, assuming a negligible change of the foreseen precipitation pattern (at least, for some of its feature) [21]. Examples of algorithms, belonging to this class, are the Tracking Radar Echoes by Correlation (TREC) [24], the Thunderstorm Identification Tracking Analysis and Nowcasting (TITAN) [6], the Storm Cell Identification and Tracking (SCIT) [10], the semi-langrangian approach proposed in [23] and those making use of spatial segmentation techniques, as in [26] and [27].

The second nowcasting class, i.e., dynamical evolution technique, allows to describe the field evolution together with their motion. Examples of dynamical evolution techniques are the McGill Algorithm for Precipitation Nowcasting by Lagrangian Extrapolation (MAPLE) [25], the Spectral Prognosis (S-PROG) [28], the COntinuiy of TREC vectors method (Co-TREC) [15], the Phase Stochastic method (PhaSt) [17], those based on autoregressive techniques, as in [30], those based on neural network, as in [4] and the CASA nowcasting system [32].

Lastly, nowcasting hybrid techniques are aimed at combining information coming from several sources, e.g., lightning detection networks, satellite observations, wind field surface measurements and numerical models. The latter being used, for example, to evaluate the convective available potential energy (CAPE) and/or the convective inhibition energy (CIN). Examples of such techniques include the GANDOLF algorithms [22], the NIMROD tool [8], [9], the National Convective Weather Forecast (NCWF) [16], the Auto NowCaster (ANC) [20], and those exploiting lighting network information as in [2].

This work addresses the problem of rain field advection, developing a new nowcasting technique, belonging to the class of extrapolation and recognition schemes. Our approach is based on the concept of spatial-scale dependence of precipitation systems, exploiting ground-based radar imagery time series. The developed nowcasting algorithm, named Spatially-adaptive Precipitation Advective Radar Estimator (SPARE), was

Manuscript received September 30, 2011; revised December 08, 2011; accepted December 19, 2011. This work was supported by the Department of National Civil Protection (DPC), Rome, Italy, under the IDRA convention.

M. Montopoli was with the Department of Electrical Engineering and Information, University of L'Aquila, 67100 L'Aquila, Italy, and with CETEMPS, University of L'Aquila. He is now with the Department of Geography, University of Cambridge, Cambridge CB2 3EN, U.K. (e-mail: mm911@cam.ac.uk).

F. S. Marzano is with the Department of Electronic Engineering, University "La Sapienza" of Rome, 00184 Rome, Italy, and with CETEMPS, University of L'Aquila (e-mail: marzano@die.uniroma1.it).

E. Picciotti is with Himet srl., 67100 L'Aquila, Italy (e-mail: errico.picciotti@himet.it).

G. Vulpiani is with the Presidency of the Council of Ministers, Department of Civil Protection, 00189 Rome, Italy (e-mail: gianfranco.vulpiani@protezionecivile.it).

Color versions of one or more of the figures in this paper are available online at http://ieeexplore.ieee.org.

Digital Object Identifier 10.1109/JSTARS.2011.2182506

preliminarily tested on some case studies observed by the Italian radar network [19].

Primary objectives of the present work can be summarized as follows: i) illustrate the SPARE algorithm methodology and optimize its computational efficiency when running on a large national radar mosaic (in other words, evaluate its operational feasibility); ii) test SPARE on a statistically significant large data set, including 31 case studies in order to compute a robust error statistics of the forecasted fields and compare them with benchmark approaches; iii) quantify the predicted uncertainty using the available information in order to provide a self-consistent quality flag. The latter concept is an original way to assign a confidence level to the nowcasting product. It is based on the automatic extraction of some spatial features of the available radar fields which can be thought to be correlated with the expected uncertainty of the foreseen images. The possibility to provide short-time precipitation field predictions accompanied by quantitative uncertainty information might open new scenarios for the operational usage of nowcasting techniques.

The paper is organized as follows. The main characteristics of the SPARE nowcasting algorithm are illustrated in Section II. A special effort is dedicated to emphasize the differences with respect to similar existing approaches. Section III describes the large amount of data, acquired by the Italian radar network, used to perform the test analysis. Finally, numerical results, expressed in terms of skill scores, are shown in Section IV, whereas the conclusions are drawn in Section V.

II. SPARE Algorithm Description

The flow diagram of the SPARE algorithm is described in Fig. 1 where the different stages of the proposed scheme are schematically shown in panels a–d. The SPARE main steps, called identification, partition, windowing, advection and application, are illustrated below, whereas some related methodological aspects are discussed in the next paragraphs of this section. We will consider the observed single-polarization radar reflectivity map $Z(x, y, t)$ where t indicates the instant of the last radar acquisition while the couple (x, y) identifies the spatial position within a Cartesian coordinate system. It is worth specifying that the SPARE technique might also be applied either to any radar polarimetric observable field or to rain-rate spatial field.

1) Identification: This step aims at identifying rain cells and their reference positions (centroids) within the observed radar reflectivity map $Z(x, y, t - \Delta t)$ at the previous instant $t - \Delta t$ where Δt is the temporal resolution. Centroids of rain cells are indicated by the couple (x_{rj}, y_{rj}) with the integer index "j" ranging from 1 to the number N_r of identified rain cells within the considered Z field. Rain cells are identified by means of a thresholding scheme, as in [18] [see Fig. 1(a) where each identified cell is contoured by a grey rectangular box]. Note that rain cells are, by definition, a set of connected pixels (i.e., pixels which are spatially contiguous) so that they can be constituted by a large number of pixels, as in the case shown in Fig. 1. Moreover note that rain cells have to satisfy some constrains in terms of rain cell average and standard deviation reflectivity to be identified. Thus some rain cells could be discarded by the identification process.

2) Partition: This step aims at partitioning rain cell centroids defined at step 1) into N_c macro-clusters whose position is described by (x_{ci}, y_{ci}) with $i \in [1, N_c]$. Centroid partitions is accomplished using a fuzzy logic "*k-means*" algorithm as explained later. The result of this step is to assign every jth rain cell centroid (x_{rj}, y_{rj}) to one of the N_c clusters located at (x_{ci}, y_{ci}).

3) Windowing: This step aims at constructing "analysis windows" for each macro-cluster identified in the previous step. The ith rectangular analysis window W_i is defined as the rectangular portion of Z which includes the ith macro-cluster [see Fig. 1(b)]. The rectangular window W_i is centered at the position (x_{wi}, y_{wi}) and, in general, it can be different from the centroid (x_{ci}, y_{ci}), the second being connected to the spatial distribution of the reflectivity field whereas the first is derived from geometrical considerations only. Radar reflectivities belonging to the analysis window W_i at time t are indicated by $Z_{Wi}(x, y, t)$.

4) Advection: This step aims at estimating the displacement vectors, respectively along the horizontal $u_{Wi} = u(x_{wi}, y_{wi})$ and the vertical $v_{Wi} = v(x_{Wi}, y_{Wi})$ direction, for each analysis window W_i. The components u_{wi}, v_{wi} are expressed in the same units of the radar grid (kilometers) or conveniently in number of pixels (if the spatial resolutions Δx along x and Δy along y are known). The displacement of each analysis window W_i is carried out using the phase correlation technique, as described in the next subsection.

5) Interpolation: This steps aims at interpolating the displacement vector components, $u(x_{Wi}, y_{Wi})$ and $v(x_{Wi}, y_{Wi})$, on the positions (x, y) of the radar grid. The output of this step is the displacement field (or advection field) of the components $u = u(x, y)$ and $v = v(x, y)$. It is worth noting that the positions (x_{Wi}, y_{Wi}) are a subset of all possible radar grid points (x, y).

6) Application: This step aims at applying the estimated displacement field components (u, v) to the last available radar acquisition $Z(x, y, t)$ at instant t for a desired number N_f of forecast time period. The following relation is used to create a time series of the predicted radar reflectivities $Z_p(x, y, t + n\Delta t)$ at the nth subsequent time step:

$$Z_p(x, y, t+n\Delta t) = Z[x-nu(x, y), y-nv(x, y), t+n\Delta t] \quad (1)$$

where Z and Z_p are expressed in dBZ, n is an integer ranging from 1 to N_f, and the temporal resolution Δt is usually expressed in minutes. When u and v are set to zero in (1), the special case of the *Eulerian persistence* is obtained [31]. Otherwise, assuming u and v constant over the considered space domain, we get the so called *Steady-State Displacement* (SSD) [23]. Within the SPARE approach the motion components u and v are position-dependent and their estimation is carried out by a new proposed correlation technique, as explained in the following section.

A. Phase Correlation

The bi-dimensional (2D) temporal cross-correlation is the most used methodology to derive the motion vector from two subsequent images or portion of them. Considering the

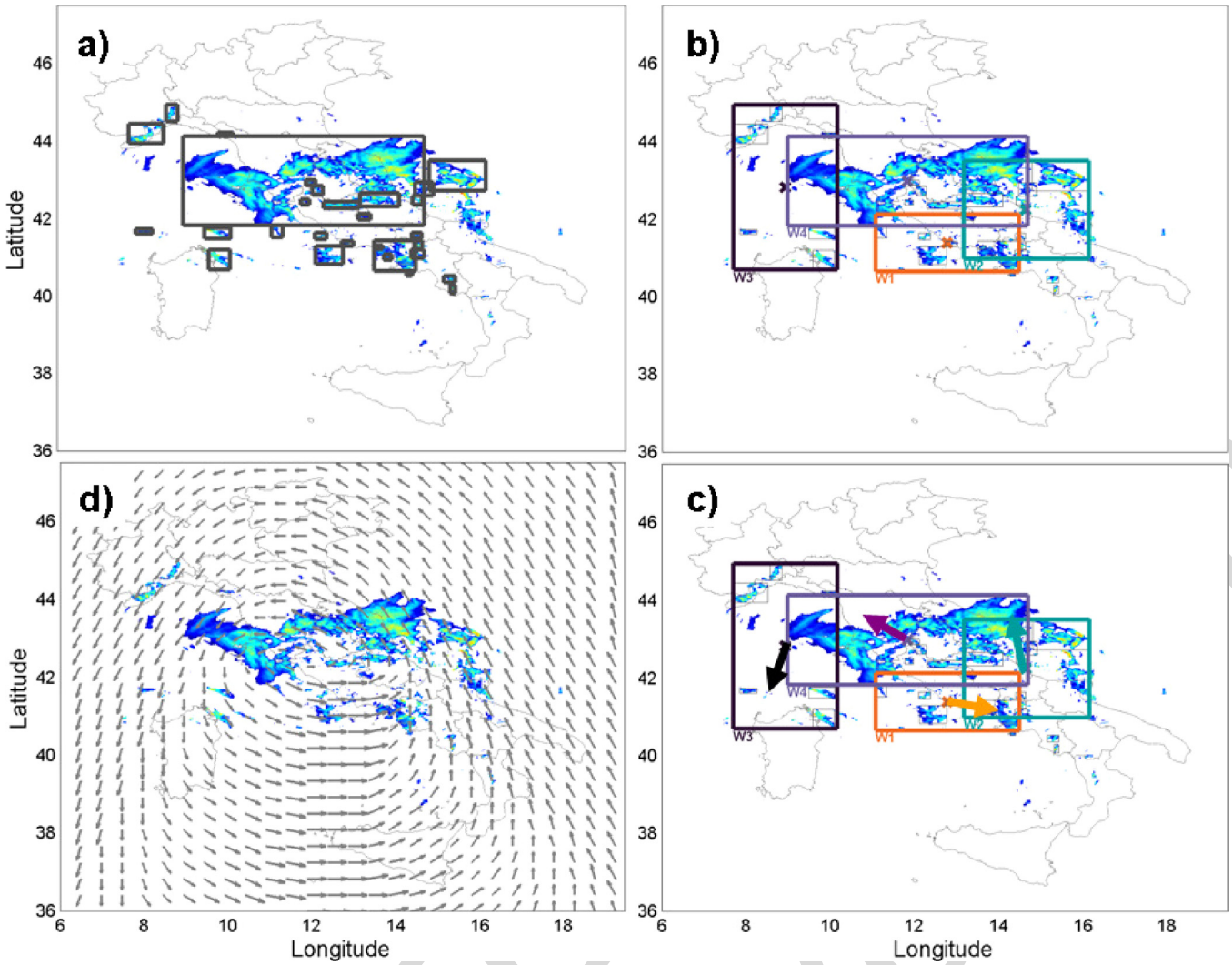

Fig. 1. Main steps of the SPARE advection scheme. (a) Rainy structure identification (gray square box). (b) Macro Cluster definition after fuzzy logic K-means clustering. (c) Displacement vectors by phase correlation. (d) Advection field by cubic Interpolation. Reflectivity is color-coded and refer to the 2-km CAPPI on November 8th, 2009, at 14:45 UTC.

reflectivity fields $Z_{Wi}(x,y,t-\Delta t)$ and $Z_{Wi}(x,y,t)$, observed respectively at $t-\Delta t$ and t, within the ith analysis windows W_i, the cross-correlation C_Z can be computed in a discrete form as

$$C_Z(\delta_x,\delta_y)=\sum_{l=1}^{L}\sum_{m=1}^{M} Z_{W_i}(x,y,t-\Delta t)Z^*_{W_i}(x-\delta_x,y-\delta_y,t) \quad (2)$$

where the symbol * indicates the complex conjugate operator, $x=l\cdot\Delta x$ and $y=m\cdot\Delta y$ are the relative Cartesian coordinates within the considered analysis window specified by the integers l and m ranging within $[1,N]$ and $[1,M]$; the integers M and L indicate the window size in terms of rows and columns of $Z_{Wi}(x,y,t-\Delta t)$ and $Z_{Wi}(x,y,t)$, respectively. The quantity $\delta_x=w\cdot\Delta x$ and $\delta_y=q\cdot\Delta_y$ are the displacements, where the integers w and q range within $[-L+1,L-1]$ and $[-M+1,M-1]$, respectively. Note that in (2), $Z_{Wi}(x,y,t)$ results to be the spatially shifted version of $Z_{Wi}(x,y,t-\Delta t)$ and, for this reason, they have the same size. In other words, the SPARE algorithm computes only one set of analysis windows at instant $t-\Delta t$ and shifts them to find a matching with the successive acquisition at instant t. The maximum of C_Z indicates the position where the two windowed fields $Z_{Wi}(x,y,t-\Delta t)$ and $Z_{Wi}(x,y,t)$ strongly match to each other thus providing the displacement between the two. When C_Z is computed, the obtained displacement vectors are associated to the positions (x_{Wi},y_{Wi}) of W_i of the whole radar map. Thus, several displacement vectors are obtained: one for each analysis window. As already mentioned, when C_Z is computed by considering the whole field $Z(x,y,t)$, instead of $Z_{Wi}(x,y,t)$ as in (2), only one displacement vector is derived and the SSD method is implicitly implemented.

Another approach to compute C_Z is based on the use of the phase of C_Z instead of its amplitude (i.e., phase cross- correlation). The need to process temporal cross-correlation by exploiting the phase feature of C_Z is motivated by the analysis of Fig. 2, where an example of the cross-correlation between two radar reflectivity maps is shown. On the right panel b) of this figure, C_Z as in (2) is used: a sort of saturation effect in proximity of the maximum is noted. Multiple maxima are possible as well, so that wrong motion directions and magnitudes

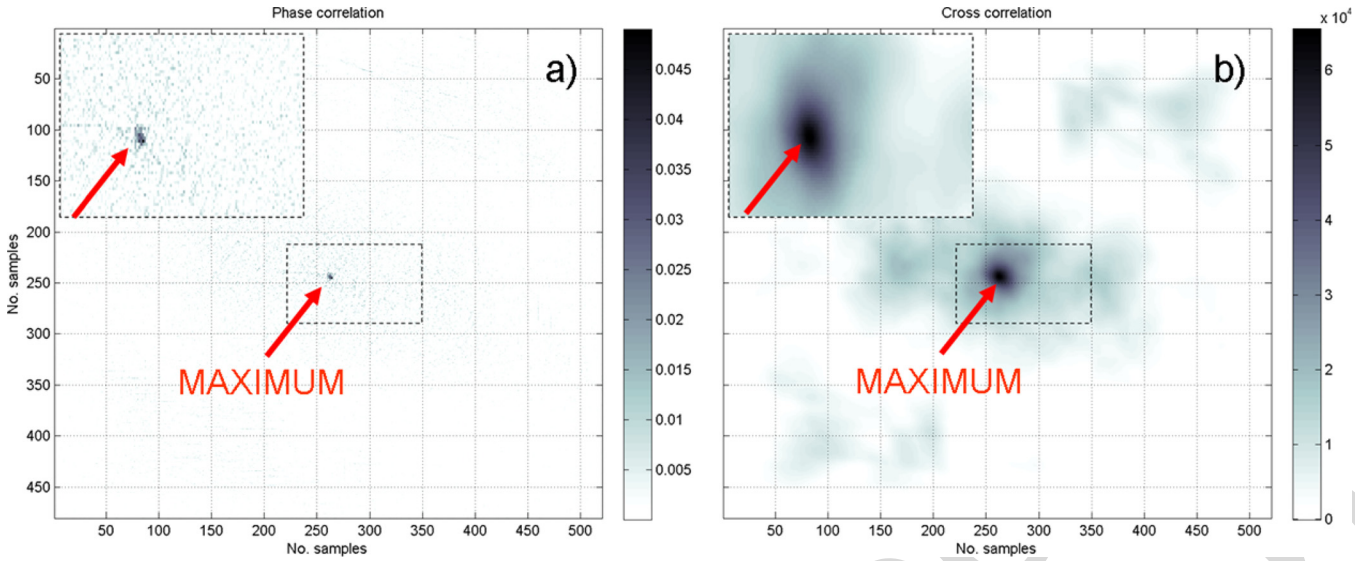

Fig. 2. Cross correlation obtained applying phase correlation method (a) and classical cross correlation (b) to the same couple or radar images . Note that color bars have been not modified and their dynamic range reflect the natural variations of cross correlation. Inset plots for each panel show the portion of correlation within the rectangular domain highlighted by dot line.

can be easily obtained. Phase cross-correlation is a possible method to overcome the problem just mentioned. Phase correlation is not a new technique [13], even though scarcely applied to radar data imagery [19]. In order to illustrate the phase cross-correlation method, it is useful to deal with the Fourier frequency domain. Resorting to the Fourier shift theorem, which states that the spatial lag (ρ_x, ρ_y) of a signal is equivalent to a phase change in the spatial frequency domain (k_x, k_y), the 2D cross correlation, expressed in (2), can be rewritten, in the special case of two subsequent inputs $Z_{Wi}(x, y, t - \Delta t)$ and $Z_{Wi}(x, y, t) = Z_{Wi}(x - \delta_x, y - \delta_y, t - \Delta t)$, as follows:

$$C_Z(\rho_x, \rho_y) = \Im^{-1}\left\{\Im\left[Z_{W_i}(k_x, k_y, t - \Delta t)\right] \cdot \Im\left[{Z_{W_i}}^*(k_x, k_y, t)\right] \cdot \exp\left[j2\pi \cdot (k_x\rho_x + k_y\rho_y)\right]\right\}. \quad (3)$$

According to (3), the displacement components (δ_x, δ_y) are accounted by the exponential term. This suggests to suppress the modulus of the exponential term in (3) and derive the following normalized phase correlation function P_Z:

$$\begin{aligned} P_Z(\delta_x, \delta_y) &= \Im^{-1}\left\{\frac{\Im\left[Z_{W_i}(k_x, k_y, t - \Delta t)\right] \cdot \Im\left[{Z_{W_i}}^*(k_x, k_y, t)\right]}{\Im[Z_{W_i}(k_x, k_y, t - \Delta t)] \cdot \Im[{Z_{W_i}}^*(k_x, k_y, t)]} \cdot \exp\left[j2\pi \cdot (k_x\delta_x + k_y\delta_y)\right]\right\} \\ &= \Im^{-1}\left\{\exp[j2\pi \cdot (k_x\delta_x + k_y\delta_y)\right\} \\ &= \delta(x - \delta_x, y - \delta_y). \end{aligned} \quad (4)$$

Relation (4) defines the phase temporal correlation method, which produces as output, a delta function of Dirac δ, centered on the searched displacements δ_x, δ_y as shown in Fig. 2(a). Note that the last term of (4) holds only if the displacement is purely linear or, in other words, no rotational components contribute to the motion. When rotational components are present, spurious contributions arise as it can be noted near the maximum in Fig. 2(a).

B. Fuzzy Logic Reflectivity Field Partition

The method used to group (or partitioning) rain cells into macro rain cell systems (or clusters) is here briefly described. The need to resort to such a partition strategy is due to the fact that the displacement field, resulting from the rain cell grouping, is more prone to represent complex situations [see, for example, the vortex shown in Fig. 1(d)]. Indeed, several tests (not shown here for brevity) have shown that, if the rain cell partitioning is not applied, the resulting displacement field becomes unstable, showing frequent spatial discontinuities which tend to deteriorate the scores of the predicted field. Otherwise, the selection of few macro clusters might provide a displacement field which is not able to describe the large variety of rainfall scenarios that are typically observed within the considered dataset.

In the following description, the maximum number of identifiable clusters is set to N_c for efficiency purposes, but the clusters are automatically formed on the basis of the spatial distribution of rain cells appearing in the current radar image.

The rain cell clustering is obtained applying the *k-means* fuzzy logic algorithm, here summarized in five steps for the sake of clarity. Fuzzy logic partition is applied to the rain cells, positioned at coordinate (x_{ri}, y_{ri}) and identified within the radar map $Z(x, y, t - \Delta t)$. The main steps are as follows.

1) Selection of a first guess of N_c centroids $(x_{ci}^{(\text{guess})}, y_{ci}^{(\text{guess})})$, chosen within rain cell positions (x_{rj}, y_{rj}) to be grouped. If the number of identified rain cells is less than N_c, the rain cells themselves constitute the desired cluster and the partition procedure stops.
2) Assignment of the rain cell centroids (x_{rj}, y_{rj}) to one of the clusters, identified at step 1), using the minimum distance criterion. The current rain cell partition is indicated by the location couple (x_{rji}, y_{rji}) which indicates the membership of the rain cell jth to the ith rain system cluster.

TABLE I
ANALYZED CASE STUDIES OF REFLECTIVITY 2 KM CAPPI TAKEN FROM THE ITALIAN WEATHER RADAR NETWORK .

No.	Date [DD MM YY]	Hour [UTC]	Duration [h]	Extension (*) [km^2]·10^4	%>40 dBZ (**) [%]	%>55 dBZ [%]
1)	01 Jan. 10	From 00:30 to 04:45	04.25	4.02	3.62	0.02
2)	07 Jan. 09	From 11:00 to 16:30	05.50	9.31	0.16	0.00
3)	26 Jan. 09	From 00:20 to 22:45	20.75	1.62	1.76	0.09
4)	03 Feb. 09	From 00:00 to 22:45	22.25	3.84	0.45	0.00
5)	07 Feb. 09	From 00:00 to 23:45	23.50	6.99	0.61	0.00
6)	31 Mar. 09	From 00:00 to 23:45	23.25	6.88	3.45	0.00
7)	01 Apr. 09	From 00:00 to 12:15	12.25	4.85	3.72	0.02
8)	15 May 09	From 00:15 to 23:45	23.50	5.97	2.73	0.01
9)	31 May 09	From 00:00 to 23:00	23.00	8.28	3.66	0.04
10)	01 Jun. 09	From 08:15 to 23:45	15.50	10.27	3.44	0.03
11)	02 Jun. 09	From 00:00 to 23:45	23.75	3.61	4.48	0.05
12)	21 Jun. 09	From 06:00 to 13:45	07.75	5.53	8.29	0.37
13)	23 Jun. 09	From 08:00 to 14:45	06.75	6.14	2.68	0.07
14)	13 Aug. 09	From 14:00 to 21:00	07.00	1.34	11.08	1.13
15)	14 Aug. 09	From 14:00 to 19:00	05.00	0.83	10.16	0.43
16)	16 Sep. 09	From 04:00 to 23:45	19.25	11.39	5.55	0.02
17)	19 Sep. 09	From 00:00 to 23:15	23.25	2.17	7.67	0.23
18)	20 Sep. 09	From 00:30 to 23:30	22.50	3.64	4.69	0.14
19)	21 Sep. 09	From 00:30 to 08:30	08.00	3.31	12.30	0.36
20)	02 Oct. 09	From 00:30 to 19:00	18.50	5.18	3.84	0.02
21)	22 Oct. 09	From 08:45 to 11:15	02.50	17.15	1.11	0.00
22)	23 Oct. 09	From 00:00 to 23:45	23.50	10.84	1.96	0.00
23)	06 Nov. 09	From 00:30 to 23:45	22.50	7.60	2.10	0.01
24)	08 Nov. 09	From 15:00 to 23:30	08.50	6.53	0.78	0.00
25)	09 Nov. 08	From 15:30 to 23:45	08.25	5.49	2.13	0.01
26)	30 Nov 09	From 02:45 to 23:00	20.00	11.40	2.67	0.01
27)	13 Dec. 09	From 11:30 to 19:00	08.00	4.60	0.06	0.00
28)	14 Dec. 09	From 15:45 to 21:30	05.50	8.05	1.20	0.00
29)	23 Dec. 09	From 00:45 to 07:30	06.50	7.23	1.54	0.01
30)	24 Dec. 09	From 07:00 to 14:00	07.00	5.56	0.40	0.00
31)	26 Dec. 09	From 07:00 to 17:45	10.75	9.94	1.69	0.00

(*) Extension of rainy systems is defined as the square kilometers covered by the reflectivity field (Z) larger than 10 dBZ.
(**) $\%Z_{th}$ is the percentage of pixels larger than the threshold Z_{th}.

3) Computation of the rain system centroids $(x_{ci}^{(\text{current})}, y_{ci}^{(\text{current})})$, given the current rain cell partition (x_{rji}, y_{rji}).
4) Repetition of steps 2) and 3) until the centroid positions $(x_{ci}^{(\text{current})}, y_{ci}^{(\text{current})})$ do not show appreciable variations below a given threshold.
5) Assignment of $x_{ci} = x_{ci}^{(\text{current})}$, $y_{ci} = y_{ci}^{(\text{current})}$.

At the end of the partitioning procedure, the obtained N_c centroids (x_{ci}, y_{ci}) and the rain cells (x_{rji}, y_{rji}) belonging to them allow to define the analysis windows, as described in Section II.

III. TEST CASES

Several storm case studies, occurred in 2009, were collected from the Italian radar mosaic, coordinated by the Italian Department of Civil Protection (DPC). The available dates, together with duration and some statistical parameters, are listed in Table I. According to the analysis accomplished by the Italian national institute of statistics (ISTAT) [1], the years 2009 and 2002 were the wettest within the decade going from 2000 to 2009. Indeed, more than 800 millimeters of average precipitation per year were registered by the Italian gauge network [1]. This consideration suggests that the collected dataset is quite representative of the rainfall regimes typically occurring in Italy.

The radar product $Z(x, y, t)$, used in this work for nowcasting purposes, consists of horizontal cuts of radar volumes (specifically CAPPI, Constant Altitude Position Plan Indicator) from the Italian radar composite at the height of 2 km above the sea level. This choice tends to mitigate the unavoidable clutter contamination due to the complex orography which characterizes northern and central Italy. Radar acquisition are available every $\Delta t = 15$ min in terms of co-polar horizontal reflectivity factor, Z with a spatial resolution $\Delta x \times \Delta y = 1$ km^2. Environmental clutter is operationally mitigated by DPC automatic procedures through a proper combination of a clear-air clutter map, an empirical visibility range-bin mask, a Doppler filtering and a spatial texture automatic analysis [29].

Among other undesired factors, which may decrease the quality of radar data mosaic, the data delivery connection timeout can play an important role. It may occasionally manifest for some radar sites with a temporal intermittent behavior (i.e., reflectivity field tend to “appear” and “disappear”). This phenomenon is deleterious when applying a nowcasting technique, such as SPARE, and can indirectly reflect into skill score analysis. This undesired effect has been soothed by visual

inspection, discarding the anomalous situations and selecting the temporal interval when this problem does not occur.

IV. Results

In this section, the error budget of SPARE predictions is evaluated by using the case study dataset, listed in Table I. This analysis is carried out from two distinct points of view. The first one is based on the classical score indexes, which are used to quantify the statistical error between SPARE predictions and radar actual observations (i.e., those radar measurements made available after their acquisitions every Δt period). This is an *a posteriori* error evaluation, which allows to globally characterize the performance of the nowcasting algorithm, but it may be less interesting within an operational framework where the uncertainty of the forecasted field should be made available when the nowcasting product is issued. The aforementioned considerations have led to the introduction of a new concept of the "uncertainty prediction", which will be described later.

The SPARE technique has been applied to a total of 1506 radar maps within the case studies listed in Table I. The initial number of clusters has been set to $N_c = 6$, the number of future steps to be forecasted has been set to $N_f = 8$ (which means a prediction period of 2 hours ahead with respect to the starting instant t). The execution time is of the order of 120 s for each run, taking into consideration that the handled maps are matrices of size 1200×1200 pixels. Tests have been performed using standard computational resources (i.e., a commercial home computer with a processor clock of 1.7 GHz and a memory of 2 GB). The source code has been developed in MatLab® environment. It is worth noting that the execution time of the proposed SPARE technique is not significantly dependent on the size of the handled radar grid because only the interpolation step is processed on a pixel basis.

A. Spare Performances

Widely used statistical skill score indicators, such as the Probability Of Detection (POD), False Alarm Rate (FAR), Critical Success Index (CSI) [21], and the Correlation Coefficient without the mean subtraction (CC) [31], are used to compare SPARE and the Eulerian persistence predictions. They are calculated for the observed Z and predicted Z_p at the forecast instants $t + n\Delta t$ and for pixels where $Z > Z_{th}$ and $Z_p > Z_{th}$ where the reflectivity threshold Z_{th} has been set to 10 dBZ. For the sake of clarity, the skill score definitions are summarized in Appendix A.

Fig. 3 shows the average trend of score indices POD, FAR, CSI and CC, as a function of the forecast lead time for all the considered case studies. SPARE and Eulerian persistence are shown in red diamond and black circles, respectively. The score index trend, shown in Fig. 3, outlines the expected worsening at increasing lead time together with an overall outperforming of SPARE with respect to the Eulerian persistence over the entire forecast period. A comprehensive comparison between SPARE and Eulerian persistence is given in Fig. 4 in terms of correlation diagram. Every forecast lead time, within the 2-hour forecast period, is considered in that figure where the 2D density distribution of occurrences is also color-coded. Fig. 4 shows that SPARE tends to outperform the Eulerian persistence, especially

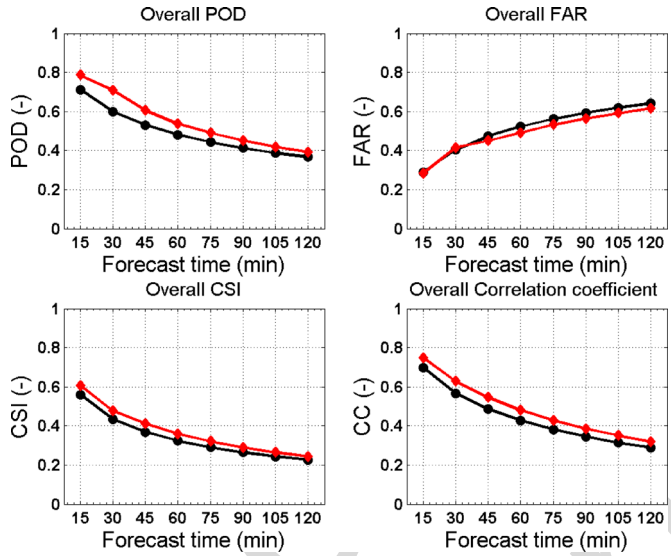

Fig. 3. Temporal average behavior of the Probability of Detection (POD), False alarm Rate (FAR), Critical Success Index (CSI) and correlation coefficient (CC) for the SPARE (red diamonds) and the Eurelian Persistence (black circles) predictions for the whole analyzed case studies.

in terms of POD, CC and CSI (note how the core part of the distribution tends to be distant from the 1–1 lines), whereas the FAR scores are more comparable.

Average values of the scores indices POD, FAR, CSI and CC for all the considered cases are listed in Table II. Average values of CSI for one hour forecast are 0.32 and 0.36 for the Eulerian persistence and SPARE, respectively, whereas for CC we have values equal to 0.43 and 0.48. Relatively to the 2-hour forecast, the average CSI decreases down to 0.21 and 0.22, respectively for the Eulerian persistence and SPARE. Regarding the average CC, it was found to decrease down to 0.31 and 0.34 for the Eulerian persistence and SPARE, respectively. Generally, there is an average improvement of 10% and 5% of SPARE with respect to the persistence for 1 and 2 hours of forecast time, respectively. Furthermore, the spreading of the scatterplots shown in Fig. 4 indicates that there are cases where SPARE performs markedly better than persistence, especially for fast time-evolving events. On the other hand, the low average values of CSI for 2-hour forecast, listed in Table II, are related to high false alarms, probably induced by the high variability of precipitation which characterize most of the Italian territory. It is worth to mention that the low values of CSI found in this work are in agreement with those obtained by other authors, e.g., [23], [17], [33].

The SPARE skill score has been analyzed in terms of seasonal trend as well. The results are shown in Fig. 5 where only average CSI for SPARE (black markers) and Eulerian persistence (grey markers) at 15 min (circles) and 120 min (squares) forecast time are shown. The highest values of the average CSI have been obtained from March to May and from September to November. Otherwise, the differences between SPARE and Eulerian persistence performances are more pronounced from March to August and tend to reduce from September to December. The minima of CSI, especially concentrated in the late winter and summer season, might be probably attributed to the long-lasting winter

TABLE II
SKILL SCORE INDEXES DEFINED BY (A.1)–(A.4) IN APPENDIX A FOR SPARE AND PERSISTENCE NOWCASTING.

Methods	POD	FAR	CSI	CC
SPARE + 1 hour	0.54	0.49	0.36	0.48
Persistence +1 hour	0.48	0.52	0.32	0.43
SPARE + 2 hour	0.39	0.61	0.22	0.34
Persistence +2 hour	0.37	0.64	0.21	0.31

POD: Probability of Detection, FAR: False Alarm Rate, CSI: Critical Success Index; CC: Correlation Coefficient without mean subtraction.

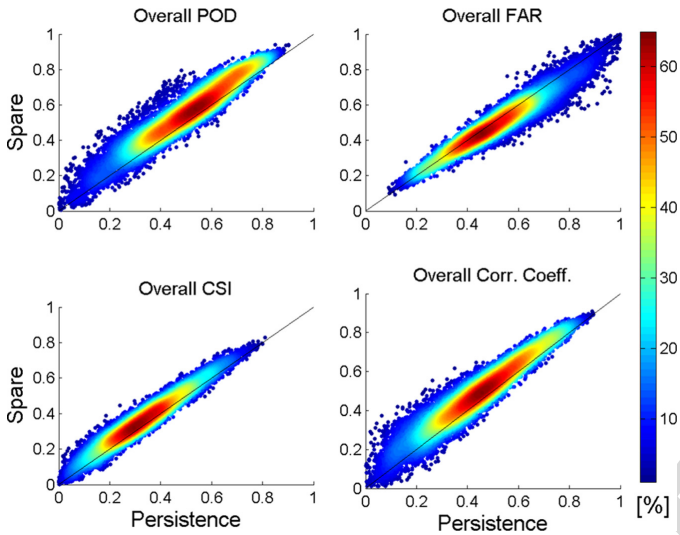

Fig. 4. Scatter plot of the Probability of Detection (POD), False alarm Rate (FAR), Critical Success Index (CSI) and correlation coefficient (CC) for the SPARE and the Eurelian Persistence predictions for the whole analyzed case studies.

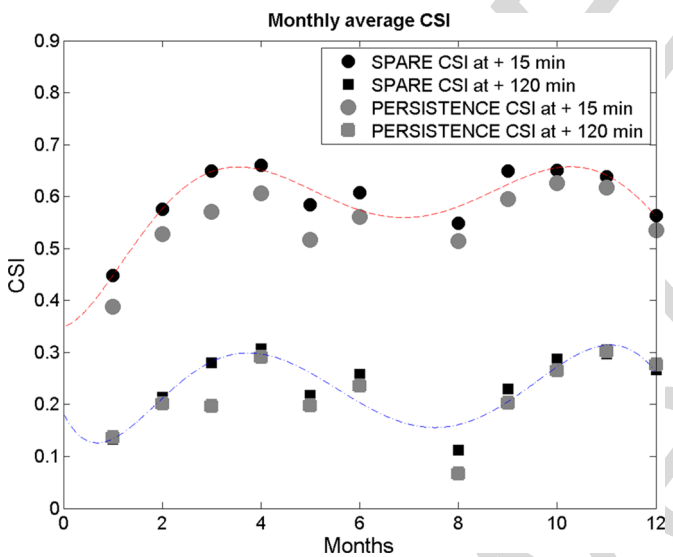

Fig. 5. Monthly average Critical Success Index (CSI) over the whole available data set for SPARE (blak markers) and Eurelian Persistence (grey markers) predictions after 15 min (circles) and 120 min (squares) from the nowcasting starting instant. Seasonal regression fit are also shown with dash-dot and dashed lines.

storms and orographically-induced summer storms. These precipitation regimes are both difficult to predict using only radar data.

B. Uncertainty Prediction

An *a priori* error budget analysis is accomplished in this section, conversely to the previous approach where skill scores were used *a posteriori* to quantify the performance of SPARE and where both Z and Z_p were considered at future instants $t + n\Delta t$. This means that for the SPARE score evaluation we can compute some features of Z at instant $t - m\Delta t$, with $\mathrm{m} = 0$ or 1, and verify whether they are related to skill scores (e.g., POD, CSI, etc.) computed at $t + n\Delta t$, once Z_p is generated. Characteristic features of $Z(x, y, t - m\Delta t)$ here considered are the texture parameters such as: Contrast (CON), Homogeneity (HOM) and Power Spectral Density (PSD) slope and the correlation coefficient (CC). The definition of the aforementioned texture parameters is reported in Appendix B.

Fig. 6 shows the results, in terms of linear correlation, for CON, HOM, PSD slope and CC computed before running SPARE with $m = 0$ (i.e., on the last available radar acquisition) and the CSI obtained after running SPARE (i.e., for n from 1 to N_f) and once the reference radar maps are available (i.e., after $N_f \cdot \Delta t$ min). For all the considered score indexes, there is a functional relation which has been parameterized as follows:

$$Y_n = a \cdot X_m^b + c \tag{5}$$

where Y_n is the CSI predicted at future instants $t + n\Delta t$ and X_m is the score index computed at previous instant t with $X = CON$ or HOM or CC or PSD slope. Regression coefficients a, b and c are listed in Table III for each combination of Y_n and X_m.

In principle, with the use of (5) and the coefficients of Table III, it is possible to estimate the SPARE expected CSI as a function of the forecast time for every generation of the SPARE-predicted radar maps. Moreover, in Fig. 6 the relation between the PSD and CSI (upper left corner of the same figure) shows that higher negative slopes (close to -3.2) correspond to higher expected values of CSI, whereas the opposite is true as well. This is in some way an expected behavior because higher PSD negative slopes mean higher spatial correlation in the space domain and than less spatial variability. Thus, the results of Fig. 6 upper left corner suggest that images with smoothed variability of reflectivity are probably easy to predict (i.e., higher CSI) with radar-based extrapolation technique like SPARE.

Eventually, in Fig. 7 a comparison between the predicted CSI, obtained through (5) before the generation of the SPARE nowcasting maps, and CSI, computed after the nowcasting generation, is shown. The various panels describe different choices of the variable X_m in (5). The prediction of CSI is in fairly good agreement with its *a posteriori* estimation with better results

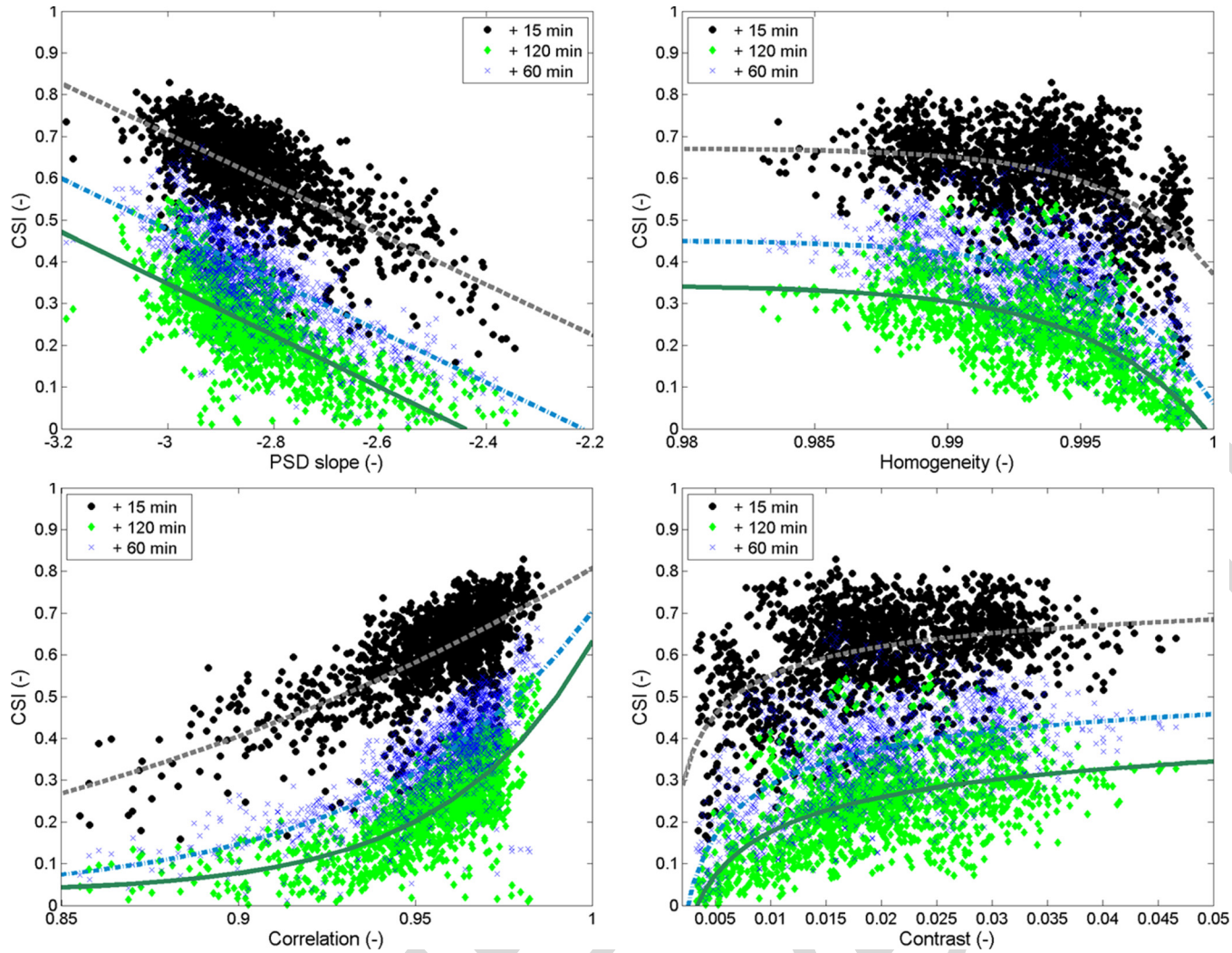

Fig. 6. Correlation diagrams between Power Spectral Density (PSD) slope, HOMogeneity (HOM), Correlation Coefficient (CC) and Contrast (CON) computed before running the SPARE procedure (on the abscissa of each panel plot) and Critical success index calculated after acquiring the reference "truth" radar maps.

TABLE III
REGRESSION COEFFICIENTS OF (5) USED TO OBTAIN THE CURVES OF FIG. 6 WHERE X_m = PSD SLOPE OR HOMOGENEITY (HOM) OR CONTRAST (CON) OR CORRELATION COEFFICIENT (CC) AND Y_n = CSI

Y_n=a·X^b_m+c	Time	a	b	c
CSI vs. PSD slope	t+1Δt	-0.60	1	-1.10
	t+4Δt	-0.61	1	-1.36
	t+8Δt	-0.62	1	-1.51
CSI vs. HOM	t+1Δt	-0.30	270.70	0.67
	t+4Δt	-0.39	251.50	0.45
	t+8Δt	-0.37	222.80	0.34
CSI vs. CON	t+1Δt	-0.04	-0.43	0.82
	t+4Δt	-0.04	-0.45	0.61
	t+8Δt	-0.10	-0.32	0.60
CSI vs. CC	t+1Δt	0.90	5.62	-0.09
	t+4Δt	0.68	16.48	0.03
	t+8Δt	0.60	24.73	0.03

when X_m = PSD or X_m = CC are used as estimators in (5). These results are encouraging and tend to confirm the potential to deal with a real-time uncertainty evaluation of precipitation nowcasting techniques.

V. CONCLUSIONS

A new nowcasting technique, named SPARE, based on a extrapolation approach, has been introduced in this work. Some original ingredients, like phase correlation and reflectivity field partition by *k-means* fuzzy logic approach, have been introduced to improve the quality and reliability of the motion field estimation. A large data set of radar reflectivity fields, for a total of 31 case studies occurred in 2009, has been considered to test the SPARE technique. It refers to the national mosaic of the Italian radar network. Such large set of radar data supports the robustness of the performed statistical analysis in terms of skill scores.

Overall results show an improvement of SPARE with respects to the Eulerian persistence reference method of about 10% and 5%, respectively, at 1 hour and 2 hours of forecast time. It is interesting to note as, in some stratiform slow evolving cases, persistence can reach high score indexes (e.g., CSI and CC up to 0.8 and 0.85, respectively) and this vanishes any efforts to bring forecast improvements with SPARE. The concept of "uncertainty prediction" has been introduced as well. Parametric relations between CSI and spatial features of the radar maps have

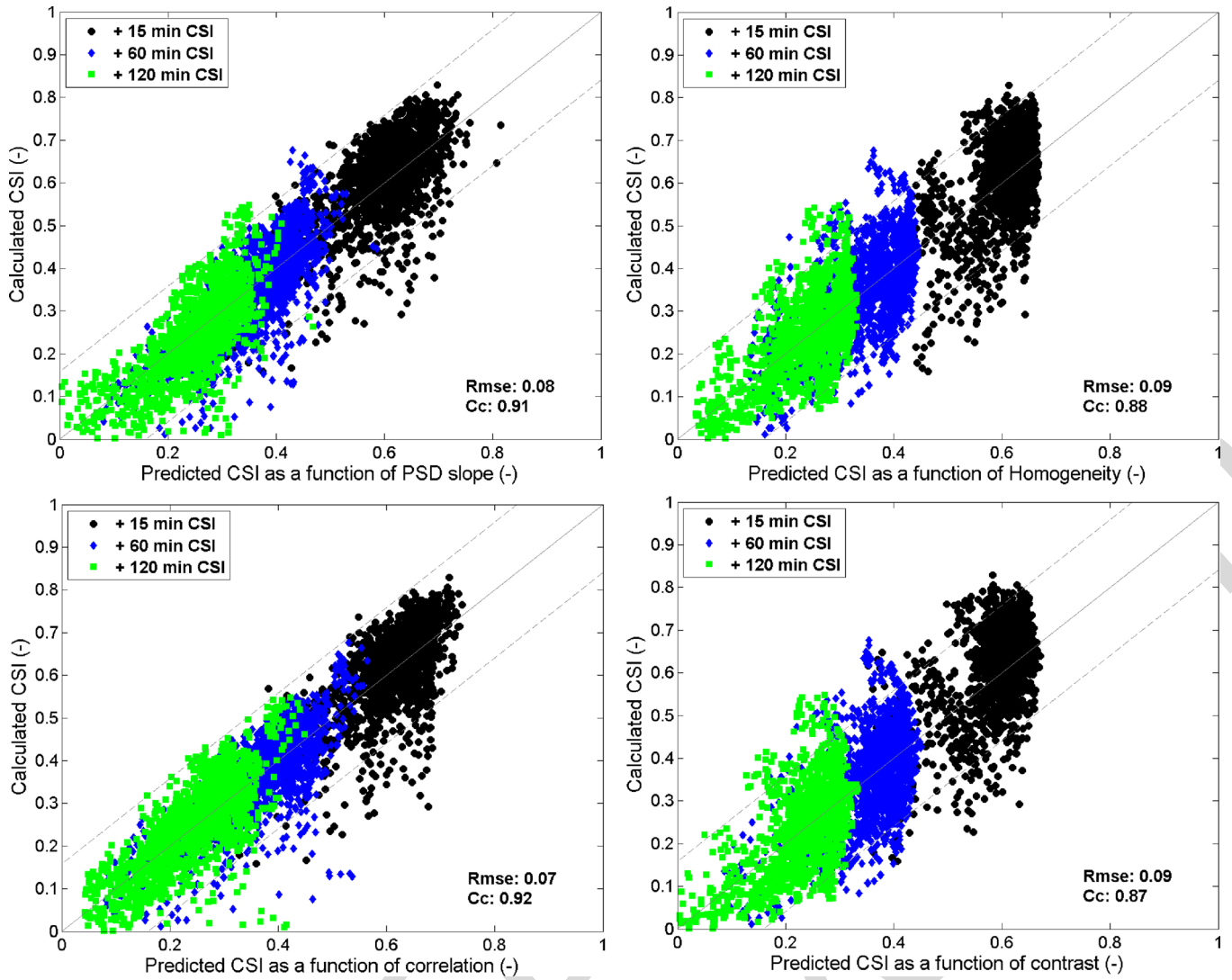

Fig. 7. Correlation diagram between the calculated CSI after running SPARE nowcasting and CSI obtained through (5) and coefficients in Table III before running SPARE nowcasting. Symbols (●), (◊), and (■) indicated CSI at forecast instant of 15, 60, and 120 m, respectively. The ± standard deviation confidence interval is also shown as grey lines above and below the bisector line.

been set up to produce the SPARE nowcasting prediction uncertainty. This allows to estimate in advance the performance of SPARE for each forecasted radar maps. A seasonal correlation of the SPARE output has been also found, suggesting that winter and summer storms may need a special effort to improve the performance of the proposed SPARE algorithm.

Future developments will be focused both on the implementation of an evolution scheme to allow changing reflectivity values with time and the inclusion of the information related to orography and seasonal dependence of the rainy systems over Italy. The use of polarimetric variables into the SPARE nowcasting scheme can also be envisaged by processing rain-rate polarimetric estimate, instead of the single-polarization radar reflectivity, as done in this work. It is not expected that this change can significantly modify the SPARE data processing steps, whereas it can improve its robustness to spatial rain field artifacts.

Appendix A
Score Indexes

This Appendix summarizes the statistical score indexes we used for comparing prediction and observations. They are the Probability Of Detection, the False Alarm Rate (FAR), the Critical Success Index, [21], and the Correlation Coefficient (CC) without the mean subtraction, [31]. To be consistent with the notation used within the text, we indicate with Z and Z_p the observed and predicted reflectivity field, respectively. Note that in general the treatment which follows is general and it is not necessarily related to reflectivity fields. POD, FAR, CSI, and CC are defined as

$$\mathrm{POD}(Z_{th}) = \frac{H}{H+M} \tag{A.1}$$

$$\mathrm{FAR}(Z_{th}) = \frac{F}{H+F} \tag{A.2}$$

$$\mathrm{CSI}(Z_{th}) = \frac{H}{H+M+F} \tag{A.3}$$

$$\mathrm{CC}(Z_{th}) = \frac{\langle Z \cdot Z_p \rangle}{\sqrt{\langle Z^2 \rangle \cdot \langle Z_p^2 \rangle}} \tag{A.4}$$

where H stands for "hit" and it is the number of pixels where Z and Z_p are both larger than a given threshold (Z_{th}); F, M, and N stand for "false", "misses" and "negatives", respectively,

and they are defined as the number of pixels where $Z \leq Z_{th}$ and $Z_p > Z_{th}$; $Z > Z_{th}$ and $Z_p > Z_{th}$; $Z > Z_{th}$ and $Z_p \leq Z_{th}$. In (A.4) the operator $\langle \cdot \rangle$ indicates the spatial average and the meaning of the dependence of "CC" by Z_{th} indicates that the Z and Z_p are conditioned to pixel position where both $Z > Z_{th}$ and $Z_p > Z_{th}$. Interval of variation of indexes in (A.1)–(A.4) are between 0 and 1 . Optimal scores are obtained when $\mathrm{POD} = 1, \mathrm{FAR} = 0, \mathrm{CSI} = 1$ and $\mathrm{CC} = 1$. For the purpose of nowcasting, both Z and Z_p in (A.1)–(A.4) are taken at the same forecast time $t + n\Delta t$ with t covering each instant of the whole available dataset and n ranging within $[1, N_f]$ at integer steps. Within the main text Z_{th} has been fixed to 10 dBZ.

Appendix B
Texture Indexes

This Appendix gives the definition of texture parameters, often used to extract information from remote sensing images. The definition of Power Spectral Density (PSD) slope is also given. To be useful, these parameters have to be extracted from maps organized in Cartesian coordinates. The texture parameters, used in this work, are the Contrast (CON) and Homogeneity (HOM) defined as

$$\mathrm{CON}(Z_{th}) = \sum_{r,c} |r-c|^2 \cdot P_{co}(r,c) \tag{B.1}$$

$$\mathrm{HOM}(Z_{th}) = \sum_{r,c} \frac{P_{co}(r,c)}{1+|r-c|} \tag{B.2}$$

where $P_{co}(r,c)$ are the elements of the co-probability matrix $\mathbf{P}_{co}$ derived from the co-occurrence matrix $\mathbf{C}_{co}$ [11], defined as the distribution of the co-occurring values within the reflectivity field Z_M, at a given spatial lag of Cartesian components l_x, l_y and with the subscript $M = \text{observed}$ or $M = \text{predicted}$ in our case. Note that the threshold Z_{th} in (B.1) and (B.2) implicates the use of values of Z_M for which $Z_M > Z_{th}$. Formally, the vales of the co-occurrence matrix $\mathbf{C}_{co}$, at row r and column c of the considered radar map can be written as follows:

$$\mathbf{C}_{co}(r,c) = \sum_{i,j} \begin{cases} 1, & \text{if } Z_M(x,y) = Z_{Mr} \text{ and } Z_M(x+l_x, y+l_y) = Z_{Mc} \\ 0, & \text{otherwise} \end{cases} \tag{B.3}$$

where Z_{Mr} and Z_{Mc} are generic discrete values of the field Z_M. The square root of the number of elements in $\mathbf{C}_{co}$ defines the number of levels in which the field Z_M is discretized before computing the co-occurrence matrix $\mathbf{C}_{co}$. Once $\mathbf{C}_{co}$ is normalized with respect to the total number of co-occurrence, a co-probability matrix $\mathbf{P}_{co}$ is obtained and it is used to extract CON and HOM in (B.1) and (B.2) for example. When the handled field is constant, $\mathrm{CON} = 0, \mathrm{HOM} = 1$. For what concerns the power spectral density, PSD, it can be estimated as

$$\mathrm{PSD}(\mathbf{k}) = \left\langle |\Im\left(Z_M(\mathbf{s})\right)|^2 \right\rangle \tag{B.4}$$

where $\mathbf{s}$ and $\mathbf{k}$ are the spatial and frequency variable vectors of components x, y and k_x, k_y, respectively, and "$\Im$" is the Fourier operator. The slope of PSD is estimated by making a linear regression on the Azimuthally Average PSD (AAPSD). This is formalizes below:

$$\mathrm{AAPSD}(|\mathbf{k}|) = \alpha \cdot |\mathbf{k}|^{\beta} \tag{B.5}$$

where β is the PSD slope to be estimated. Previous equation is justified by considering that AAPSD usually decreases following a power law [17].

Acknowledgment

A special acknowledgment is given to the HIMET (L'Aquila, Italy) staff and, in particular, to Dr. K. De Sanctis for his strong support in storing and providing radar data. Prof. B. De Berardinis (ISPRA, Italy) and Eng. P. Pagliara (DPC, Italy) are gratefully acknowledged for their support. Radar data of the Italian national mosaic have been obtained from the National Department of Civil Protection (DPC, Rome, Italy, www.protezionecivile.it/) through the IDRA project (cetemps.aquila.infn.it/idra), managed by the Centre of Excellence CETEMPS (L'Aquila, Italy, cetemps.aquila.infn.it) and technically operated by HIMET (L'Aquila, Italy, www.himet.it/).

References

[1] C. Abate and L. Salvati, "Andamento Meteo-Climatico in Italia, Anni 2000–2009," (in Italian) Ambiente e Territorio, Istituto nazionale di statistica (ISTAT), Rome, Italy, 2010 [Online]. Available: www.istat.it/salastampa/comunicati/non_calendario/20100401_00

[2] P. N. Blossey, C. S. Bretherton, J. Cetrone, and M. Khairoutdinov, "Cloud-resolving model simulations of KWAJEX: Model sensitivities and comparisons with satellite and radar observations," *J. Atmos. Sci.*, vol. 64, pp. 1488–1508, 2007.

[3] P. Bonelli and P. Marcacci, "Thunderstorm nowcasting by means of lightning and radar data: algorithms and applications in northern Italy," *Nat. Hazards Earth Syst. Sci.*, vol. 8, pp. 1187–1198, 2008.

[4] C. Marzban and G. Stumpf, "A neural network for for tornado prediction based on doppler radar-derived attributes," *J. Appl. Meteor*, vol. 35, pp. 617–626, 1996.

[5] R. Daley, *Atmospheric Data Analysis*. Cambridge, U.K.: Cambridge Univ. Press, 1991.

[6] M. Dixon and G. Weiner, "TITAN: Thunderstorm identification, tracking analysis and nowcasting a radar based methodology," *J. Atmos. Ocean. Technol.*, vol. 10, pp. 785–797, 1993.

[7] M. S. Gilmore, J. M. Straka, and E. N. Rasmussen, "Precipitation uncertainty due to variations in precipitation particle parameters within a simple microphysics scheme," *Mon. Weather 25 Rev.*, vol. 132, pp. 2610–2627, 2004.

[8] B. W. Golding, "NIMROD, A system for generatine automated very short range forecasts," *Meteor. Appl.*, vol. 5, pp. 1–16, 1998.

[9] B. Golding, "Quantitative precipitation forecasting in the UK," *J. Hydrol.*, vol. 239, pp. 286–305, 2000.

[10] J. T. Johnson, P. L. MacKeen, A. Witt, E. D. Mitchell, G. J. Stumpf, M. D. Eilts, and K. W. Thomas, "The storm cell identification and tracking algorithm: An enhanced WSR-88D algorithm," *Weather Forecast.*, vol. 13, pp. 263–276, 1993.

[11] R. M. Haralick and K. Shanmugam, "Textural features for image classification," *IEEE Trans. Syst., Man, Cybern.*, vol. 3, no. 6, pp. 610–621, 1973.

[12] E. Kalnay, *Atmospheric Modeling, Data Assimilation and Predictability*. Cambridge, U.K.: Cambridge Univ. Press, 2003.

[13] C. Kuglin and D. Hines, "The phase correlation image alignment method," in *Proc. Int. Conf. Cybernetics and Society*, 1975, pp. 163–165.

[14] F. Lalaurette, "Early detection of abnormal weather conditions using a probabilistic extreme forecast index," *Quart. J. Royal Met. Soc.*, vol. 129, pp. 3037–3057, 2003.

[15] L. Li, W. Schmidt, and J. Joss, "Nowcasting of motion and growth of precipitation with radar over a complex orography," *J. Appl. Metereol.*, vol. 34, pp. 1286–1300, 1995.

[16] D. Megenhardt, C. K. Mueller, N. Rehak, and G. Cunning, "Evaluation of the national convective weather forecast product," in *Preprints 9th Conf. Aviation, Range, and Aerospace Meteorology, Amer. Met. Soc.*, Orlando, FL, 2000, pp. 171–176.
[17] S. Metta, J. V. Hardenberg, L. Ferraris, N. Rebora, and A. Provenzale, "Precipitation nowcasting by a spectral-based nonlinear stochastic model," *J. Hydrometeorol.*, vol. 10, pp. 1285–1297, 2009.
[18] M. Montopoli and F. S. Marzano, "Maximum likelihood retrieval of modeled convective rainfall patterns from mid-latitude C-band weather radar data," *IEEE Trans. Geosci. Remote Sens.*, vol. 45, no. 7, pp. 2403–2416, Jul. 2007.
[19] M. Montopoli, F. S. Marzano, G. Vulpiani, V. Poli, and P. P. Alberoni, "An improved spectral-dynamical technique for rain field nowcasting from radar image time series," in *Proc. 5th Eur. Radar Conf.*, Helsinki, Finland, 2008.
[20] C. T. Muller, S. R. Roberts, J. Wilson, T. Betancourt, S. Dettling, N. Oien, and J. Lee, "NCAR Autonowcast system," *Weather Forecast.*, vol. 18, pp. 445–561, 2003.
[21] C. E. Pierce, E. Ebert, A. W. Seed, M. Sleigh, C. G. Collier, N. I. Fox, N. Donaldson, J. W. Wilson, R. Roberts, and C. K. Mueller, "The nowcasting of precipitation during Sydney 2000: An appraisal of the QPF algorithms," *Amer. Met. Soc.*, vol. 19, pp. 7–21, 2004.
[22] C. E. Pierce, C. G. Collier, P. J. Hardaker, and C. M. Haggett, "GANDOLF: A system for generating automated nowcasts of convective precipitation," *Meteorol. Applicat.*, vol. 8, pp. 341–360, 2000.
[23] V. Poli, P. P. Alberoni, and D. Cesari, "Intercomparison of two nowcasting methods: Preliminary analysis," *Meteorol. Atmos. Phys.*, vol. 101, pp. 229–244, 2008.
[24] R. E. Rinehart and T. Garvey, "Three dimensional storm motion detection by conventional weather radar," *Nature*, vol. 9, pp. 273–287, 1978.
[25] B. Turner, I. Zawadzki, and U. Germann, "Scale dependence of the predictability of precipitation from continental radar images. Part III: Operational nowcasting implementation (MAPLE)," *J. Appl. Meteor.*, vol. 43, pp. 231–248, 2004.
[26] V. Lakshmanan and T. Smith, "Data mining storm attributes from spatial grids," *J. Ocean Atmos. Technol.*, vol. 26, no. 11, pp. 2353–2365, 2009.
[27] V. Lakshmanan, R. Rabin, and V. DeBrunner, "Multiscale storm identification and forecast," *J. Atm. Res.*, vol. 67, pp. 367–380, Jul. 2003.
[28] A. Seed, "A dynamical and spatial scaling approach to advection forecasting," *J. Appl. Meteorol.*, vol. 42, pp. 381–388, 2003.
[29] G. Vulpiani, P. Pagliara, M. Negri, L. Rossi, A. Gioia, P. Giordano, P. P. Alberoni, R. Cremonini, L. Ferrarsi, and F. S. Marzano, "The Italian radar network within the national early-warning system for multi-risks management," in *Proc. 5th Eur. Conf. Radar in Meteorology and Hydrology ERAD 2008*, 2008.
[30] K. Xu, C. K. Wikle, and N. I. Fox, "A Kernel-based spatio-temporal dynamical model for nowcasting weather radar reflectivities," *J. Amer. Statist. Assoc.*, vol. 100, no. 472, pp. 1133–1144, 2005.
[31] I. Zawadzki, "Statistical properties of precipitation patterns," *J. Appl. Meteor.*, vol. 12, pp. 459–472, 1973.
[32] E. Ruzanski, V. Chandrasekar, and Y. Wang, "The CASA nowcasting system," *J. Atmos. Ocean. Technol.*, vol. 28, no. 5, pp. 640–655, May 2011.
[33] L. Han, S. Fu, L. Zhao, Y. Zheng, H. Wang, and Y. Lin, "3D convective storm identification, tracking, and forecasting—An enhanced TITAN algorithm," *AMS*, vol. 26, pp. 719–732, Apr. 2009.

Mario Montopoli received the Laurea degree in electronic engineering from the University of L'Aquila, L'Aquila, Italy, in 2004, and the Ph.D. degree in radar meteorology in a joint program between the University of Basilicata, Potenza, Italy, and the Sapienza University of Rome, Rome, Italy, in 2008.

In 2005, he joined the Centro di Eccellenza per l'integrazione di Tecniche di Telerilevamento e Modellistica Numerica per la Previsione di Eventi Meteorologici Severi as a Research Scientist on ground-based radar meteorology with a special focus on C-band applications and processing techniques. Since 2006, he has been with the Department of Electrical and Information Engineering, University of L'Aquila, as a Research Assistant. Since October 2011, he has been with the Department of Geography at the University of Cambridge, U.K., as a Marie Curie Fellow. His main interests are on precipitation retrieval from meteorological events and volcanic eruptions, C-band radar applications and processing techniques, spaceborne radiometry for Earth and planetary observations.

Dr. Montopoli was the recipient of the best paper award in the European Radar Conference held in Sibiu, Romania, in 2010.

Frank Silvio Marzano (S'89–M'99–SM'03) received the Laurea degree (*cum laude*) in electrical engineering (1988) and the Ph.D. degree (1993) in applied electromagnetics, both from *La Sapienza* University of Rome, Italy.

After being with the Italian Space Agency (ASI) and a lecturer at the University of Perugia, Italy, in 1997 he joined the Department of Electrical Engineering and co-founded the Center of Excellence CETEMPS, University of L'Aquila, Italy. In 2005 he joined the Department of Electronic Engineering (now the Department of Information Engineering, Electronics and Telecommunications), *La Sapienza* University of Rome, Italy, where he presently teaches courses on antenna theory, electromagnetic propagation and remote sensing. Since 2007, he has also been Vice-Director of CETEMPS, University of L'Aquila, Italy. His current research concerns passive and active remote sensing of the atmosphere from ground-based, airborne, and spaceborne platforms, development of inversion methods, radiative transfer modeling of scattering media and radar meteorology issues. He is also involved in radio and optical propagation topics in relation to incoherent wave modeling, scintillation prediction and rain fading analysis along terrestrial and satellite links.

Dr. Marzano has published more than 100 papers on international refereed journals, 30 book chapters and 200 extended abstracts in conference proceedings. He co-edited two books on remote sensing in 2002 and 2010. He is a reviewer for the major international journals in remote sensing, geoscience and propagation. Since January 2004, he has been an Associate Editor of IEEE *Geoscience and Remote Sensing Letters*; since 2011 he has also been an Associate Editor of EGU *Atmospheric Measurement Techniques*. In 2005 and 2007 he was a Guest Co-Editor of the MicroRad04 and MicroRad06 Special Issues for IEEE TRANSACTIONS ON GEOSCIENCE AND REMOTE SENSING. He is a Senior member of the IEEE Geoscience and Remote Sensing Society. In 1993 he received the Young Scientist Award of XXIV General Assembly of URSI (Osaka, Japan). In 1998 he was the recipient of the ARPAD award from the Naval Research Laboratory (Washington, DC), and in 2008 he received the Best Paper Award from the EGU-Plinius Conference (Nicosia, Cyprus) and in 2009 the Best Oral Paper Award on propagation from the EuCAP Conference (Berlin, Germany). During 2001–2005 he was the Italian national delegate for the European COST actions n. 720 and n. 280; since 2008 he has been the national delegate for the European COST Action project ES702 "EGCliMet" and COST Action project IC0802 "PropTNEO". Since 2010 he has been a member of the European Volcanic Ash Cloud Expert Group (EVACEG).

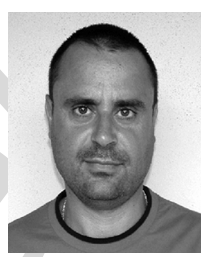

Errico Picciotti received the Laurea degree (*cum laude*) in electrical engineering in 1992 from the University of Ancona, Italy.

In 1997 he joined the Science and Technology Park of Abruzzo, L'Aquila, Italy as a radar meteorologist. In 2002 he became a researcher within the Center of Excellence CETEMPS, working on radar systems and polarimetry. Since 2007 he has been working with HIMET, L'Aquila, Italy, becoming coordinator of the Radar Meteorology Division.

Gianfranco Vulpiani (M'06) received the Laurea degree in physics and the Ph.D. degree in radar meteorology from the University of L'Aquila, L'Aquila, Italy, in 2001 and 2005, respectively.

In 2001, he was with the Department of Physics and the Center of Excellence CETEMPS, University of L'Aquila, where he was a Research Scientist on ground-based radar meteorology, with special focus on C-band applications and polarimetric applications. He was a Visiting Scientist with Colorado State University, Fort Collins, in 2004. In 2006,

he was with the Department of Observation Systems, Météo-France, Paris, France, where he was a Postdoctoral Researcher.Within the framework of the European project FLYSAFE, he has worked on the development of dual-polarization retrieval techniques with a special focus on attenuation correction and hail detection. Since March 2007, he has been with the Department of Civil Protection, Rome, Italy, where he is in charge of the scientific coordination of the Italian radar network. He is a Reviewer for several international journals in remote sensing topics.